

# Theoretical Analysis of Non-Catalytic Growth of Nanorods on a Substrate

S. Joon Kwon\*

Materials Science and Technology Division, Korea Institute of Science and Technology (KIST), P.O. Box 131, Cheongryang, Seoul, 130-650, Korea

Received: October 30, 2005; In Final Form: December 19, 2005

A theoretical analysis explaining the whole process of the growth of nanorods on a substrate without a catalyst is presented. Prior to the growth of the nanorods, the reaction precursors form nuclei on the substrate. The nuclei undergo cluster migration caused by the surface diffusion of adatoms on the substrate, and this migration continues until the mean free time of the adatoms is larger than surface diffusion time. The most probable mechanism by which cluster migration takes place is the one that leads to the minimization of the cluster free-energy, namely the migration of six adatoms into one fixed adatom. This cluster migration continues during several (typically smaller than 6) consecutive nuclei growth steps. After the process of cluster migration comes to an end, the nuclei grow in an isotropic manner by collection of the adatoms, until the nucleus reaches the thermodynamic size limit. The one-dimensional growth of nanorods on the nuclei, which is associated with the critical radius, begins when the reactant dose is smaller than a certain value, which is determined by the thermodynamic size limit and the mass transport parameter. The mass transport of the reaction precursors leads to the expansion of the radius and elongation of the height of the nanorods, and the growth rate of the height is greater than that of the radius. This difference in the growth rate causes the aspect ratio to increase with increasing growth time. By comparing the experimental data in the literature (ZnO nanorods), the presented analysis explains well the noncatalytic growth of nanorods on a substrate.

## I. Introduction

The synthesis of nanometer-scale materials has been the subject of intense interest in the recent decade. These nanomaterials (NMs) are of particular interest, since they provide the means to advance both their practical potentiality and academic frontiers. The theoretical aspects of NMs need to be addressed in more detail to keep up with the rapid synthetic progress. In the case of the formation of one-dimensional (1D) NMs,<sup>1–5</sup> several studies have explained why 1D NMs have the optimal radius,<sup>6,7</sup> why they grow normal to the amorphous surface,<sup>8</sup> why they have the maximum aspect ratio<sup>8</sup> and growth kinetics involving relationships between the growth rate and the radius,<sup>9</sup> and the catalytic growth of nanowires.<sup>10</sup> Although these studies provided useful models to reveal certain aspects of the formation and growth of the 1D NMs, there have been few studies which attempted to explain how they form on the substrate without a catalyst and why they grow with an elongated shape in the equilibrium state. Significance of the noncatalytically grown 1D NMs originates from their sharp morphology and from well-aligned uniform arrays by which one can use them in a multitude of future electronic device applications. The noncatalytic process allows a readier regiment of the feature size of 1D NMs, since it is not governed by the nanoscale size or curvature<sup>9,10</sup> of the catalytic materials. To obtain a deeper insight into the noncatalytic formation of 1D NMs and to utilize these materials in a controllable manner, a theoretical analysis is needed.

In the present study, we provide a theoretical analysis on the growth process of 1D NMs, focusing on single crystalline 1D nanorods, which grow unidirectionally on the substrate without catalyst in a vapor-phase transport synthetic system. This

analysis excludes the case of the formation of nanorods via the vapor–liquid–solid (VLS) mechanism in conjunction with the formation of a metal catalyst–nanorod alloy.<sup>1–4,10,11</sup> It also does not consider the probability of multi-axial growth and curved elongation of the nanorods. From these points of view, our work should be distinguished from studies involving the use of thermodynamic and kinetic models to explain the growth of nanowires by the VLS mechanism.<sup>6,7,10</sup> We also assumed that the vapor-phase system is at a high enough reaction temperature to allow the surface diffusion of small nuclei on the substrate, along with a relatively low pressure to lead to a slow growth rate. Our analytical model was compared with the recent experimental data on the growth of semiconductor nanorods and we found that most aspects of the growth of the nanorods could be explained by our model.

## II. Theoretical Framework and Discussions

**2.1. The Early Stages of the Formation of the Nuclei.** In the early stages of the formation of the nuclei for the growth of the nanorods, the growth of the nuclei hinges on the initiation of the adatoms (refer to Figure 1a and b). These adatoms are comprised of reaction precursors adsorbed onto the substrate followed by the phase transition from the gaseous state to the solid adatoms. The mean free time of the adatoms on the substrate is expressed as  $\tau = \exp(E_D/kT)/\nu$ ,<sup>12</sup> where  $E_D$  is the desorption energy of the adatom from the substrate,  $k$  is the Boltzman constant,  $\nu$  is the vibration frequency of the adatom, and  $T$  is the surface temperature of the substrate. Settled adatoms have a spherical shape, which is associated with a projected radius onto the surface,  $r_1 = R_1 \sin \theta$ , where  $R_1$  is the effective radius (refer to Figure 1) and  $\theta$  is the contact angle of the adatom on the substrate. Because the feature sizes of the settled adatoms are smaller than the size of several atoms, there exists a critical

\* To whom correspondence should be addressed: phone: +82-2- 958-5504, fax: +82-2-958-5489; e-mail: cheme@kist.re.kr.

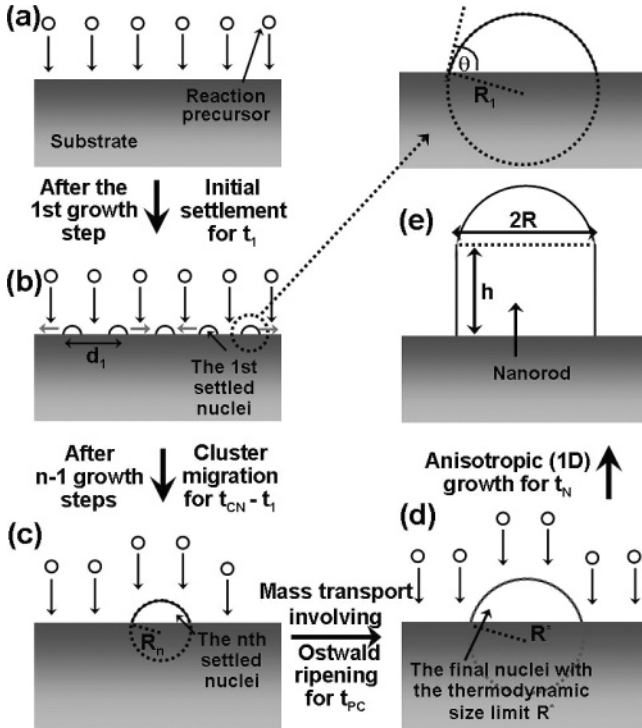


**Figure 1.** Schematic illustration of the whole growth process of nanorods on a substrate, without a catalyst, by the vapor-phase transport reaction.

inter distance,  $d_1$ , at which a certain array of the settled adatoms is energetically favored. For the sake of simplicity, this adatoms array was approximated to a 6-fold coordinated hexagonal lattice with an average lattice constant,  $d_1$ , as illustrated in Figure 2a. During the first settlement (the nucleation delay in the first growth step),  $t_1$ , this lattice is covered with the adatoms in conjunction with an effective transport flux that is responsible for the net mass transport of the reaction precursor to the substrate,  $N_1$  (adatoms/m<sup>2</sup>s). After the first growth step, the first settled adatoms choose the way to reduce their free energy, which normally involves the surface diffusion of the adatoms and their subsequent merging with each other (Figure 1c). Assuming that  $T$  is high enough, this surface diffusion mainly hinges on the translation of the adatoms along the substrate. Cluster migration competes with Ostwald ripening for the surface diffusion. If the size distribution of the first settled adatoms is narrow enough, it is reasonable to assume that the surface diffusion of the adatoms follows cluster migration rather than Ostwald ripening. The latter process is better suited to an array of adatoms with a relatively wide size distribution.<sup>13,14</sup> Therefore, cluster migration of the adatoms along the substrate can be assumed to be carried out concurrently.

In the second growth step, the cluster migration of the first settled adatoms on the substrate can involve various numbers of migrating adatoms, such as 2 (cluster migration mode 2, Figure 2b), 3 (mode 3, Figure 2c) or 6 (with one fixed adatom, mode 6, Figure 2d). To determine which mode governs the cluster migration, we calculated the probabilities for each migration mode. In each mode, the probabilities for the migration in a certain cluster array,  $P_i$ , where  $i$  is the mode number (2, 3, or 6) can be determined by considering the difference in the free energy before and after the cluster migration per unit cell in each mode,  $\Delta F_i$ , and  $E_D$ . The first settled adatoms can choose from among 12 different ways (refer to Figure 2a) in which to move in the 6-fold coordinated hexagonal lattice. In cluster migration mode 2,  $P_2$  can be

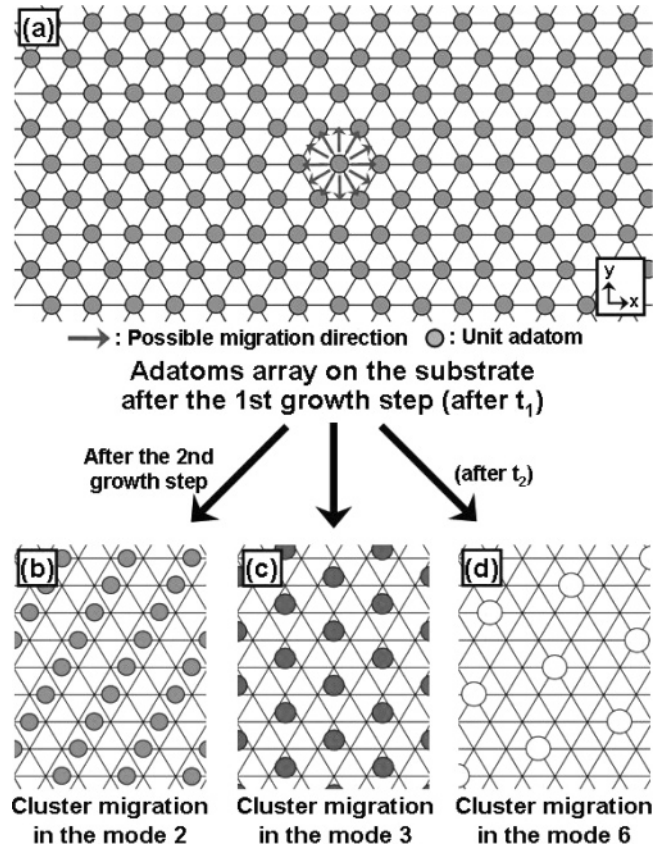


**Figure 2.** Schematic illustration of the first settled adatoms array (gray circles) on the substrate with a 6-fold coordinated hexagonal lattice (a). Each adatom can migrate in 12 different possible translation directions (12 arrows in a). Cluster migration of these first settled adatoms can be carried out by three kinds of migration manners: two adatoms migration (cluster migration mode 2, b), three adatoms migration (cluster migration mode 3, c), and six adatoms migration to one fixed adatom (cluster migration mode 6, d).

calculated as follows:

$$P_2 = \left[ \left( \frac{1}{12} \right)^2 \exp \left( \frac{-2E_D}{kT} \right) \left\{ 1 - \exp \left( \frac{\Delta F_2}{kT} \right) \right\} \right]^{n_2} \quad (1)$$

where  $n_2$  is the average number of unit cells per fixed surface area of the substrate,  $A'$ , after the cluster migration in mode 2. The first settled adatoms are allocated on the substrate according to the minimized free energy of the total array given by the Lennard–Jones (LJ) 6–12 potentials. Then,  $\Delta F_2$  is equal to the sum of the free energy gain afforded by the difference in the LJ potentials due to the variance of the inter distance caused by the migration,  $\Delta F_{2LJ}$ , and the free energy loss by the merging of the adatoms,  $\Delta F_{2surf}$ .  $\Delta F_{2LJ}$  is expressed as  $\Delta F_{2LJ} = 5(A/d_1^6 - B/d_1^{12})$ , and  $\Delta F_{2surf}$  is  $\Delta F_{2surf} = \pi\gamma R_1^2(1 - \cos\theta)(2 + \cos\theta)(2^{2/3} - 2)$ , where  $\gamma$  is the surface tension of the adatom. Calculating the LJ potential with typical values of the attractive and repulsive force coefficient,  $A \sim 10^{-77}$  Jm,<sup>6</sup> and  $B \sim 10^{-134}$  Jm<sup>12</sup>,<sup>15</sup> respectively, with values of  $R_1 \sim 1/2 (B/A)^{1/6} \sim 1.58 \times 10^{-10}$  m,  $d_1 \sim (2B/A)^{1/6} \sim 3.55 \times 10^{-10}$  m, and  $\gamma = 5 \times 10^{-1}$  Jm<sup>-2</sup>, we found that  $\Delta F_{2surf}$  exceeds  $\Delta F_{2LJ}$  by 3 orders of magnitude. Therefore,  $P_2$  can be rewritten as follows:

$$P_2 \approx \left[ \left( \frac{1}{12} \right)^2 \exp \left( \frac{-2E_D}{kT} \right) \left\{ 1 - \exp \times \left\{ \frac{\pi\gamma R_1^2(1 - \cos\theta)(2 + \cos\theta)(2 - 2^{2/3})}{kT} \right\} \right\} \right]^{A'/\sqrt{3}d_1^2} \quad (2)$$

where it should be noted that  $n_2 = A'/\sqrt{3}d_1^2$ . Similarly,  $P_3$  and  $P_6$  are written as follows:

$$P_3 \approx \left[ \left( \frac{1}{12} \right)^3 \exp \left( \frac{-3E_D}{kT} \right) \left[ 1 - \exp \times \left\{ -\frac{\pi\gamma R_1^2 (1 - \cos\theta)^2 (2 + \cos\theta)(3 - 3^{2/3})}{kT} \right\} \right] \right]^{2A'/3} \sqrt{3}d_1^2$$

and

$$P_6 \approx \left[ \left( \frac{1}{12} \right)^6 \exp \left( \frac{-6E_D}{kT} \right) \left\{ 1 - \exp \left( \frac{-E_D}{kT} \right) \right\} \left[ 1 - \exp \times \left\{ -\frac{\pi\gamma R_1^2 (1 - \cos\theta)^2 (2 + \cos\theta)(7 - 7^{2/3})}{kT} \right\} \right] \right]^{2A'/7} \sqrt{3}d_1^2 \quad (3)$$

To compare these probabilities, the probability ratios were calculated and we found that the cluster migration mode 6 (the surface diffusion of six surface adatoms into one fixed adatom (7-fold coalescence)) is the most probable way in which migration occurs to form the merged nuclei, since  $A'/\sqrt{3}d_1^2 \gg 1$ . To calculate the probability ratios, typical values of  $E_D$ ,  $E_D = 5 \times 10^{-1}$  eV,<sup>12</sup> was used such at fixed temperature  $T = 1000$ K.

**2.2. Formation of the Nuclei during Cluster Migration of the Adatoms.** During the cluster migration mode 6, the surface diffusion is known to be governed by several parameters viz. the process temperature, the effective radius of the adatom after the  $n$ th growth step,  $R_n$ , and the surface diffusion free energy,  $E_{sd}$ . The coalescence of the settled nuclei in sequential growth steps results from this surface diffusion. The surface diffusion coefficient on the substrate,  $D_{sd1}$  (subscript 1 means the first growth step) is expressed as,  $D_{sd1} = (C/R_1^s) \exp(-E_{sd}/kT)$ , where the exponent  $s$  ranges from 1 to 3 and  $C$  is a constant.<sup>12,16</sup> Therefore, the migration time taken for the second growth step,  $t_2$ , is written as  $t_2 = d_1^2/D_{sd1}$ . After  $t_2$ , the volume of the second settled adatom is equal to the sum of the volumes of the incident precursor adatoms and the volume of the first nuclei formed by the merging of the 7-fold adatoms in the first growth step. The effective radius of the nuclei after the second growth step  $R_2$  is written as,  $R_2 = R_1 \{ 7\sqrt{3}t_2 N_2 d_1^2/2 + 7 \}^{1/3}$ , where  $N_2$  is the effective flux of the incident adatoms supplied to the reaction for the second growth step (numbers/m<sup>2</sup>s). In a similar way, the effective radius of the  $n$ th nuclei after the  $n$ th growth step  $R_n$  can be generalized as follows:

$$R_n = R_1 \left\{ 7^{n-1} \left( \sum_{k=2}^n \frac{\sqrt{3}N_k t_k d_1^2}{2} + 1 \right) \right\}^{1/3} \quad (4)$$

In eq 4, the effective flux for the  $k$ th growth step,  $N_k$ , can be written as follows:

$$N_k = \frac{2N_1}{7^{k-1}\sqrt{3}d_1^2} \left[ \left\{ \frac{7^{k-1}\sqrt{3}d_1^2}{2} - 7\pi R_{k-1}^2 \sin^2\theta \right\} \left\{ 1 - \exp \times \left( \frac{-E_D}{kT} \right) \right\} + 7\pi R_{k-1}^2 \sin^2\theta \left\{ 1 - \exp \left( \frac{-E_D}{kT} \right) \right\} \right] \quad (5)$$

where  $E_D'$  is the desorption energy of one adatom on another adatom at  $T$ . For the sake of simplicity,  $E_D'$  is assumed to be  $E_D$ , and then, eq 5 is rewritten as  $N_k \approx 2\sqrt{3}/3t_1 d_1^2$  based on the fact that  $\sqrt{3}N_1 t_1 d_1^2/4 \{1 - \exp(-E_D/kT)\} = 1/2$ , and then, eq 4 reads as the following:

$$R_n = R_1 \left[ 7^{n-1} \left\{ \frac{d_1^2}{t_1 D_{sd1}} \left( \frac{7^{(n-1)(1+(s/3))} - 1}{7^{(1+(s/3))} - 1} \right) + 1 \right\} \right]^{1/3} \quad (6)$$

In a similar way, the total growth time for the formation of the  $n$ th nuclei after  $n$  consecutive steps,  $t_{CM}$ , can be generalized as follows:

$$t_{CM} = t_1 + \frac{d_1^2}{D_{sd1}} \left[ \frac{7^{(n-1)(1+(s/3))} - 1}{7^{(1+(s/3))} - 1} \right] \quad (7)$$

In Figure 3, the relationships between  $R_n$  and the order of the serial growth steps,  $n$  (eq 6), and between the normalized growth time,  $(t_{CM} - t_1)/t_1$ , and  $n$  (eq 7) are presented. As is apparent from the figure,  $R_n$  and  $(t_{CM} - t_1)/t_1$  increase rapidly with the  $n$  increase. Particularly, in the early growth steps,  $R_n$  increases relatively slowly with a growth rate of  $7^{1/3}$ , while in the final growth steps ( $n \geq 5$ ),  $R_n$  increases very quickly with a growth rate of  $7^{(2+(s/3))/3}$ . This growth behavior of  $R_n$  indicates that the growth of the nuclei is mainly caused by the cluster migration in the early growth steps, while in the later growth is mainly accomplished by mass transport involving collection of the smaller incident adatoms. In contrast to the behavior of  $R_n$ ,  $(t_{CM} - t_1)/t_1$  increases with a nearly constant rate of  $7^{1+(s/3)}$ . The growth of the nuclei affected by the cluster migration does not continue for a long time, and it should be determined when cluster migration will cease.

**2.3. Nucleation Stage after the Cessation of the Cluster Migration.** Knowing when the cluster migration of the surface adatoms will stop is important, because this provides information about the average number density of the surface nuclei and the resulting nanorods on the substrate. Cluster migration ceases when the migration time of the incident precursor adatoms (with the effective radius of  $R_1$ ) is larger than  $\tau$ . If the migration time is larger than  $\tau$ , the spontaneous migration of the incident adatoms toward the settled nuclei is no longer favorable, since the incident adatoms will choose to coalesce with themselves or to desorb from the substrate. Insufficient migration time inhibits the migration, since the surface free energy is not minimized and the settled adatoms desorb prior to merging. Thermodynamic aspect of the cessation of the cluster migration can be addressed by considering free energy variation. During the  $n + 1$ th growth step, the incident adatoms of  $m$  units on the substrate can partially or totally merge with each other or with the settled nuclei of radius  $R_n$ . The surface free energy can be compared with each representative stage of merging, viz. before the merging ( $F_{S1}$ ), the total merging of incident adatoms with each other ( $F_{S2}$ ), and the merging of whole incident adatoms with the settled nuclei ( $F_{S3}$ ).  $F_{Si}$  ( $i = 1, 2$ , or  $3$ ) can be expressed as follows:

$$\begin{aligned} F_{S1} &= f(\theta)(R_n^2 + mR_1^2), F_{S2} = f(\theta)(R_n^2 + m^{2/3}R_1^2), \\ F_{S3} &= f(\theta)(R_n^3 + mR_1^3)^{2/3} \\ f(\theta) &= \frac{\pi\gamma(1 - \cos\theta)^2(2 + \cos\theta)}{\sin^2\theta}, \\ m &= \left( 7^{n-1}d_1^2 - \frac{2\pi R_n^2}{\sqrt{3}\sin^2\theta} \right) \frac{7^{(n-1)(1+(s/3))}}{3t_1 D_{sd1}} \quad (8) \end{aligned}$$

Comparing  $F_{Si}$ , the merging of whole incident adatoms with the settled nuclei is the most energetically favorable; therefore, cluster migration no longer continues when the migration time



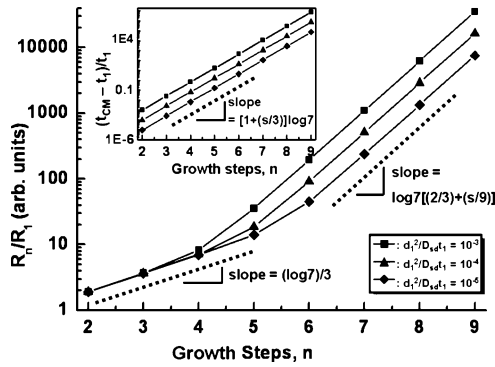


**Figure 3.** Relationship between the order consecutive growth step,  $n$ , and the ratio of the effective radius of the nucleus after the  $n$ th growth step,  $R_n$ , to the effective radius of the first settled adatom,  $R_1$ , for different values of  $d_1^2/(t_1 D_{sd1})$ , where  $d_1$  is the inter distance between neighboring adatoms after the first growth step,  $D_{sd1}$  is the surface diffusion coefficient on the substrate in the first growth step, and  $t_1$  is the time for the first settlement of the adatoms on the substrate. The exponent of  $R_n$  in the relationship between  $R_n$  and the surface diffusion coefficient of the nucleus during the  $n$ th growth step,  $D_{sdn}$ , such that  $D_{sdn} \propto 1/R_n^s$  was assumed to be 2. Inset shows the relationship between  $n$  and the normalized growth time  $(t_{CM} - t_1)/t_1$ , where  $t_{CM}$  is the total growth time of the nucleus for the consecutive merging of the adatoms after  $n$  steps.

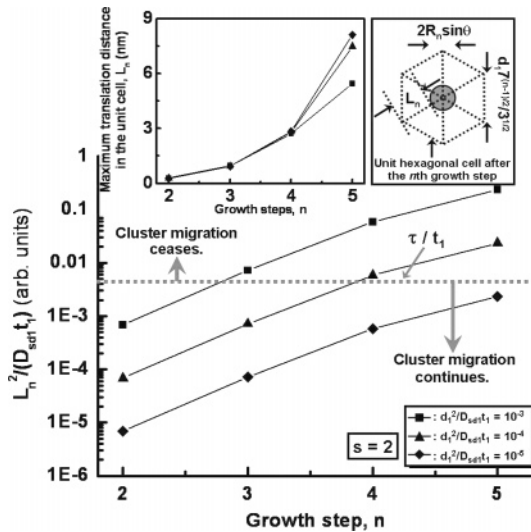


**Figure 4.** Relationship between  $n$  and  $L_n^2/(D_{sd1} t_1)$ , where  $L_n$  is the maximum translation distance of the adatom on the substrate by the surface diffusion for different values of  $d_1^2/(t_1 D_{sd1})$ . When the ratio between the mean free time of the adatom on the substrate,  $\tau$ , and  $t_1$  (dashed line) is larger than  $L_n^2/(D_{sd1} t_1)$ , cluster migration ceases. Left inset is for the relationship between  $n$  and  $L_n$  for different values of  $d_1^2/(t_1 D_{sd1})$ . Right inset is a schematic illustration showing the unit hexagonal cell including the nucleus in the center (circle) after the  $n$ th growth step.

is larger than  $\tau$ . The maximum migration time of the incident adatom after the  $n$ th growth step (refer to the right inset of Figure 4) can be calculated such that  $L_n^2/D_{sd1}$ , where  $L_n$  is the maximum translation distance of the adatom ( $L_n = \{7^{(n-1)/2} d_1 / \sqrt{3}\} - R_n \sin \theta$ ). Therefore, the cluster migration ceases when following inequality is satisfied:

$$\frac{\{7^{(n-1)/2} d_1 / \sqrt{3}\} - R_n \sin \theta}{D_{sd1} t_1} > \frac{\tau}{t_1} \quad (9)$$

The value of  $\tau/t_1$  can be obtained using typical values of the reaction parameters,  $t_1 \sim 5 \times 10^{-2}$  s,<sup>12,17</sup> and  $\tau \sim 3 \times 10^{-4}$  s,<sup>12</sup>

and it is found to be  $\tau/t_1 \sim 6 \times 10^{-3}$ . In Figure 4, a relationship between  $L_n^2/(D_{sd1} t_1)$  and  $n$  was shown. In the plots, cluster migration continues below the dashed line ( $\tau/t_1 \sim 6 \times 10^{-3}$ ). From the figure, the nuclei growth step accompanying the cluster migration will cease when  $n$  is larger than 6.

The growth process of the nuclei after the cessation of the cluster migration (Figure 1d) is only caused by the mass transport involving Ostwald ripening of the incident adatoms. During the post cluster migration growth time  $t_{PC}$ , the effective radius of the resulting adatoms,  $R_{PC}$ , is equal to  $[R_n^3 + 7^{n-1} t_{PC} \pi (1 - \cos \theta)^2 (2 + \cos \theta) R_1^3 / 3 t_1]^{1/3}$ . The post cluster migration growth of the nuclei continues until  $R_{PC}$  reaches the thermodynamic limit (minimum threshold) of the size of the nuclei ( $R^*$ ). Based on the theory for the heterogeneous nucleation,  $R^*$  is determined as  $R^* = -(2\gamma/\Delta G)$ , where  $\Delta G = -(kT/\Omega) \ln(P/P^E)$  is the chemical free-energy change of the phase transformation of the nucleus per unit volume of the nucleus,  $\Omega$ , and  $P$  and  $P^E$  are the supersaturated partial pressure and the equilibrium vapor pressure of the nucleus at  $T$ , respectively.<sup>6,7,12,18</sup>

**2.4. Formation of the Nanorods on the Nuclei after Reaching the Thermodynamic Size Limit.** After reaching the thermodynamic size limit  $R^*$ , the growth of the nuclei can proceed by two possible mechanisms: isotropic expansion or anisotropic (1D) growth. The growth mechanism, which is followed, depends on whether the momentary volume of the incident adatoms,  $\delta V$ , is greater than a certain threshold volume. This threshold, which determines the growth mechanism, can be calculated by comparing the surface energy gains in each case. Crystalline effects such as growth rate of different crystal facets, the mismatched lattice energy, stacking faults, etc. are not considered here, since those effects are much smaller than the thermodynamic effects in the noncatalytic growth 1D nanorods.<sup>8</sup> The surface energy gains of the rod-shape nucleus ( $\delta F_1$ ) and the isotropically expanded nucleus ( $\delta F_2$ ) given by an increase in the volume,  $\delta V$ , can be written as  $\delta F_1 = 2\pi\gamma R^{*2} (1 - \cos \theta) + 2\gamma\delta V/R^* \sin \theta$  and  $\delta F_2 = 2\pi\gamma (1 - \cos \theta) [3\delta V/\pi(1 - \cos \theta)^2 (2 + \cos \theta) + R^{*3}]^{2/3}$ , respectively. Then, by comparing the free energy ratio,  $\delta F_1/\delta F_2$  with unity, one can determine whether the nucleus grows in an isotropic or an anisotropic manner after its radius attains the critical value,  $R^*$ . In Figure 5, the theoretical behavior of  $\delta F_1/\delta F_2$  as a function of  $\delta V/R^{*3}$  is shown for the value of  $\theta$  of  $60^\circ$ . When the value of  $\delta V/R^{*3}$  is smaller than the critical value,  $\delta V_C/R^{*3}$  ( $\delta F_1/\delta F_2 = 1$  when  $\delta V_C/R^{*3} = 2.65$  with  $\theta = \pi/3$ ), the nucleus chooses anisotropic growth, while it grows in an isotropic manner when  $\delta V/R^{*3}$  is larger than  $\delta V_C/R^{*3}$ .  $\delta V_C/R^{*3}$  can be calculated by equating  $\delta F_1$  and  $\delta F_2$ . As was plotted in the inset of Figure 5,  $\delta V_C/R^{*3}$  is smaller than 3.03 without reference to  $\theta$ . Therefore, a reaction with a relatively slow supply (smaller reactant dose satisfying the condition of  $\delta V_C/R^{*3} < 3.03$ ) of the reaction precursors is more likely to lead to an anisotropic morphological transition than that with a fast supply. In other words, a growth rate lower than about  $2R^*$  per unit time is more favorable for the growth of nanorods. Consequently, this anisotropic growth mechanism yields the rod-shaped structure.

It is notable that whether the nanorod has an anisotropic structure or not is solely determined by the dimensionless parameter governed by the nanoscale curvature,<sup>9,10</sup>  $R^*$ , given by classical thermodynamics. Although the deeper thermodynamic consideration on the nucleation is required for  $R^*$ ,<sup>19</sup> it is well-known that  $R^*$  increases with the increases of  $T$ ,<sup>6,19</sup> and  $\gamma$ . According to classical thermodynamics, an isotropic structure is more energetically favorable than anisotropic one, at the initial

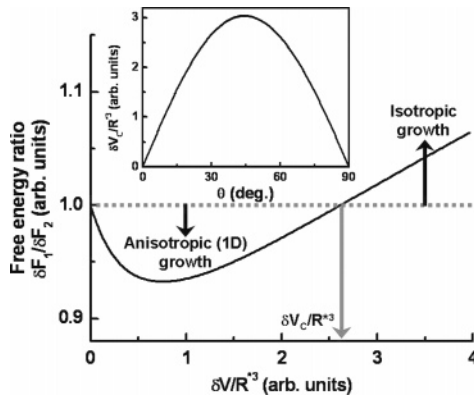


**Figure 5.** Relationship between the volume ratio,  $\delta V/R^3$  ( $\delta V$  is the momentarily provided volume of the reaction precursors to the structure and  $R^*$  is the thermodynamic limit of the effective radius of the nucleus on the substrate) and the surface free-energy ratio,  $\delta F_1/\delta F_2$  (subscript 1 is for the nucleus growing in an anisotropic manner (1D growth) and 2 is for the nucleus growing in an isotropic manner) when  $\theta = \pi/3$ . Note that the anisotropic growth is favored when  $\delta V/R^3 < \delta V_c/R^3$  ( $\delta F_1/\delta F_2 = 1$  when  $\delta V/R^3 = 1$ ). Inset is for the relationship between the contact angle of the nucleus on the substrate,  $\theta$ , and  $\delta V_c/R^3$ .

stages of nucleation when  $\gamma$  is large enough. As opposed to this classical behavior in the case of a thin film or of the bulk, structural anisotropy is advantageous with the larger  $R^*$  resulting from the greater value of  $\gamma$  for the morphological transition at the nanoscale level.

**2.5. Growth of the Nanorods: Growth Rates of the Radius and Height.** Once the nuclei select the anisotropic growth manner (Figure 1e), the increase in volume afforded by the continuous supply of the reaction precursors contributes to increases in two feature sizes of the nanorods: the radius and the height. The preferential growth direction of the nanorods is determined to have the minimum free energy, and this growth direction is normal to the surface of the substrate in most cases of the homogeneous nucleation.<sup>8</sup> The free energy comprises the surface energy<sup>8,20</sup> and the strain energy.<sup>21</sup> As referred to above in section 2.4, the surface energy governs the initial stage of the anisotropic growth in which an isotropic nucleus is transformed into an anisotropic structure. After the initial stage, the strain energy determines not only the preferential growth direction, but also the feature sizes of the nanorods. The supply of the reaction precursors can be simplified to two directions, viz. the axial ( $a$ -direction) and the radial directions ( $r$ -direction), as shown in Figure 6a. We excluded the other possible supply direction assuming that the amount of precursor particles supplied to the side of the nanorods is negligible due to the protection provided by the vertical rod structure. This exclusion is mainly attributed to the nanoscale dimensions and array of the rods, since the boundary layer for the mass transport of the reactants ( $\delta \sim L_S/Re^{1/2}$ , where  $L_S$  is the length of the substrate and  $Re$  is the Reynolds number)<sup>12</sup> exceeds the inter distance and feature sizes of the nanorods by 5 or 6 orders of magnitude. This is also based on the good step coverage given by low-pressure metal–organic chemical.<sup>12</sup> Both supply mechanisms contribute to the growth of the radius and height of the nanorods, and the possible mechanisms by which the feature sizes are increased and are quantitatively determined by examining the probabilities for four different kinds of growth: (1) axial supply leading to an increase in the height ( $P_{aa}$ ), (2) axial supply leading to an increase in the radius ( $P_{ar}$ ), (3) radial supply leading to an increase in the height ( $P_{ra}$ ), and (4) radial supply leading to

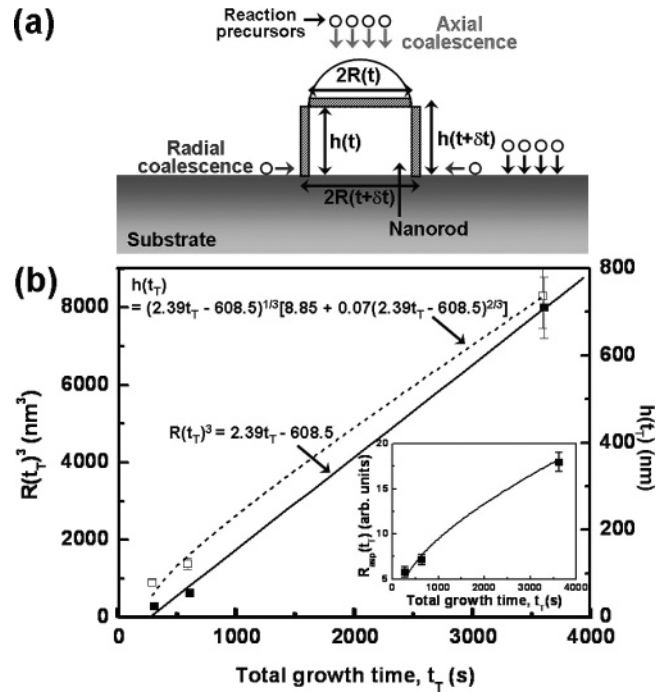


**Figure 6.** Schematic illustration for the growth of the nanorods on the substrate after infinitesimal reaction duration,  $\delta t$  (a). Oblique lined regions result from the mass transport of the reaction precursor particles during  $\delta t$ . The growth of the nanorods is attributed to two mass transport mechanisms: the axial and the radial supplies of the reaction precursor particles with the nanorods. Comparisons of the experimental data of ZnO nanorods synthesized by low-pressure MOCVD (LP–MOCVD) grown on the substrate without a catalyst reported in the literature<sup>4</sup> with the theoretical predictions (b). Dark symbols are experimental data of the radius as a function of the total growth time of the nanorods ( $t_T$ ),  $R(t_T)$  (fitted with the solid line), and open symbols are experimental data of the height,  $h(t_T)$  (fitted with the dashed line), of the nanorods. Lower inset shows that the experimental data of the aspect ratio ( $R_{asp}(t_T)$ ) of the ZnO nanorods (dark symbols) is also matched well with the theoretical prediction (solid line).

an increase in the radius ( $P_{rr}$ ).  $P_{ij}$  can be expressed as follows:

$$P_{ij} = \frac{\exp\left(-\frac{\Delta E_{ij}}{kT}\right)}{\sum_{i,j} \exp\left(-\frac{\Delta E_{ij}}{kT}\right)}, \Delta E_{ij} = \Delta E_{Sij} + \Delta E_{Tij}, i, j = a, r \quad (10)$$

In considering the free energy gain in each case ( $\Delta E_{ij}$ ), we assumed that the radius of the nanorods is thick enough to guarantee a much smaller surface energy gain,  $\Delta E_{Sij}$ , than the strain energy gain,  $\Delta E_{Tij}$ . In each case,  $\Delta E_{Tij}$  can be written as follows:

$$\Delta E_{Taa} = E_m(1 - \sigma_m)\epsilon_a^2, \Delta E_{Tar} = E_m\sigma_m\epsilon_a^2, \Delta E_{Tra} = E_m\sigma_m\epsilon_r^2, \Delta E_{Trr} = E_m(1 - \sigma_m)\epsilon_r^2 \quad (11)$$

where  $E_m$  is the elastic modulus,  $\sigma_m$  is the Poisson's ratio of the nanorod (we assumed that the feature size of the nanorods is large enough to guarantee continuum mechanical properties of the structure), and  $\epsilon_i$  is the strains in the axial ( $i = a$ ) and radial directions ( $i = r$ ). During the infinitesimal reaction duration,  $\delta t$ , the volume additivities in each direction (refer to Figure 6a) can be expressed as follows:

$$f(\theta) = \frac{(1 - \cos\theta)^2(2 + \cos\theta)}{3} \quad (12)$$

$$h(t)R(t)\frac{\partial R(t)}{\partial t} = \frac{\sqrt{3}f(\theta)R_1^3}{3t_1d_1^2} \left[ P_{ar}R(t)^2 \sin^2 \theta + P_{rr} \left\{ \frac{7^n d_1^2 \sqrt{3}}{14} - R(t)^2 \sin^2 \theta \right\} \right]$$

$$R(t)^2 \frac{\partial h(t)}{\partial t} = \frac{2\sqrt{3}f(\theta)R_1^3}{3t_1d_1^2} \left[ P_{aa}R(t)^2 \sin^2 \theta + P_{ra} \left\{ \frac{7^n d_1^2 \sqrt{3}}{14} - R(t)^2 \sin^2 \theta \right\} \right]$$

From eq 12, we obtained the following differential equation pertaining to  $R(t)$ ,

$$R(t)^3 \frac{\ddot{R}(t)}{\dot{R}(t)^2} \sin^2 \theta \left( 1 - \frac{P_{ar}}{P_{rr}} \right) + R(t)^2 \sin^2 \theta \left\{ 2 \left( \frac{P_{aa}}{P_{rr}} - \frac{P_{ar}}{P_{rr}} \right) - \left( 1 - \frac{P_{ar}}{P_{rr}} \right) \right\} + \frac{R(t)\ddot{R}(t)}{\dot{R}(t)^2} \frac{7^n \sqrt{3} d_1^2}{14} + \frac{7^n \sqrt{3} d_1^2}{14} \left( 1 + \frac{P_{ra}}{P_{rr}} \right) = 0, \dot{R}(t) = \frac{\partial R(t)}{\partial t} \quad (13)$$

An analytic solution of eq 13 cannot be obtained; therefore, we solved the equation by assuming that the difference in the strain energy in each of the four growth cases is negligible, and the approximate solution can be expressed as follows:

$$R(t_N) \approx (C_1 t_N + R^{*3})^{1/3} \quad (14)$$

where  $t_N$  is the growth time of the nanorods since the moment when the isotropic nuclei start to grow in an anisotropic manner (1D direction) and  $C_1$  is a constant that is dependent on the reaction conditions. Interestingly, the form of  $R(t)$  corresponding to the approximate growth rate is also observed in the growth kinetics of semiconductor nanoparticles that can be explained by the Lifshitz–Slyozov–Wagner (LSW) theory for the diffusion-limited coarsening of small particles.<sup>13,14,22,23</sup> The approximate solution of  $h(t)$  can also be obtained using eqs 14 and 12 as follows:

$$h(t_N) \approx \frac{\sqrt{3}f(\theta)R_1^3 R(t_N)}{C_1 t_1} \left[ \frac{7^n \sqrt{3} P_{rr}}{14} + \frac{\sin^2 \theta (P_{ar} - P_{rr}) R(t_N)^2}{d_1^2} \right] \quad (15)$$

Because  $R(t_N)$  increases monotonically with increasing  $t_N$ , the aspect ratio of the nanorods,  $R_{asp}(t_N) = h(t_N)/2R(t_N)$ , also increases with increasing  $t_N$ , since  $P_{ar}$  is not strictly equal to  $P_{rr}$ , and  $R(t_N)$  is much larger than  $d_1$ . An increase in  $R_{asp}(t_N)$  indicates that the growth of the nanorods favors the axial growth direction more than the radial growth direction, and that the growth of the nanorods in the anisotropic direction continues until the aspect ratio limit is reached.

**2.6. Comparison with Experiment.** To assess the validity of the presented model, we compared our analysis with recent representative experimental data reported by Park et al. about the growth of ZnO nanorods on a sapphire substrate.<sup>4</sup> In the above-mentioned report, no catalyst was used, and the feature size distribution of the nanorods grown normal to the surface by the vapor-phase transport reaction was quite narrow. And the growth of the ZnO nanorods mainly hinged on LP–MOCVD

vapor deposition (LP–MOCVD) with the relatively slower supply of reactants. The low-pressure condition for the vapor-phase deposition is favorable for the nanorods growth over a large area with uniform geometry.<sup>12</sup> The relatively slower supply is compatible with the condition suggested in our analysis, in which a relatively smaller reactant dose is responsible for the anisotropic structure growth. Although the mass transport of reactants increases with the reaction pressure decrease, the flow rate of reactants is much smaller than that in the case of deposition of a thin film. Comparing synthetic conditions for the ZnO thin film and nanorods, the flow rates in the case of thin film deposition exceeds those in the case of nanorods by 1–4 orders of magnitude.<sup>24</sup> The experimental data on the growth rate of the nanorods was compared with our model for the time period starting when the nuclei on the substrate start to grow in an anisotropic manner (after the pre-nanorods growth duration,  $t_{pre} = t_{CM} + t_{PC}$ ). As is apparent from Figure 6b, the experimental data concerning the radius of the ZnO nanorods is well matched with our model given by eqs 14 and 15. The value of the constant  $C_1 = 2.39(\text{nm}^3\text{s}^{-1})$  in eq 14 can be obtained by fitting the data with our model. The total growth time of the nanorods,  $t_T$ , comprises  $t_{pre}$  and  $t_N$ , and the fitting also gives the value of  $R^{*3} - 2.39t_{pre} = -608.5 (\text{nm}^3)$ . With these values, we found that the experimental data concerning the height of the ZnO nanorods was also well matched with our model given by eq 15, as shown in Figure 6b. The fitting gives the values of the constants in eq 15  $f(\theta)R_1^3 7^n P_{rr}/t_1 = 98.7(\text{nm}^3\text{s}^{-1})$  and  $f(\theta)\sin^2 \theta (P_{ar} - P_{rr})/d_1^2 t_1 = 0.097(\text{nm}^{-2}\text{s}^{-1})$ . From these fitting constants, with typical values of  $\theta = 60^\circ$ ,  $R_1 = 1.58 \times 10^{-10}\text{m}$ ,  $d_1 = 3.55 \times 10^{-10}\text{m}$ ,  $n = 3$ , and  $P_{rr} \sim 1/4$ , we found that  $P_{ar} - P_{rr} \sim 10^{-6}$ , which is also congruent with the approximation made in eq 13. Another value calculated from the fitting,  $t_1 \sim 10^{-3}\text{s}$ , is a factor of 10 times lower than  $t_1$  used in our model (refer to section 2.3).<sup>17</sup> This difference in the value of  $t_1$  might be due to the fact that the effective growth rate of the nuclei during the first nucleation delay is greater than that in LP–MOCVD.

As shown in the inset of Figure 6b, the aspect ratio of the ZnO nanorods,  $R_{asp}$ , can be predicted from eqs 14 and 15 with the fitted constants, and the experimental values of  $R_{asp}$  is well matched with the predicted values. In the inset, one can also find that  $R_{asp}$  increases as the nanorods grow. This behavior of the growth rate of the nanorods indicates that there exists a preferential orientation of the uniaxially grown nanorods due to several factors including preferred crystalline direction, asymmetric sticking coefficient, etc.<sup>1–4</sup> The structural limit of  $R_{asp}$  is determined by  $\kappa = (W_a/\gamma) - 1$ , where  $W_a$  is the work of adhesion required to separate an individual nanorod from the substrate. In the equilibrium state, the maximum value of  $R_{asp}$  as a function of  $\kappa$ ,  $R_{asp,max}$  can be written as follows:<sup>8</sup>

$$R_{asp,max} = \frac{16\{F(\kappa)\}^3}{3}, F(\kappa) = \frac{\{12\gamma + 8 + (144\kappa^2 + 192\kappa)^{1/2}\}^{1/3} + \{12\gamma + 8 - (144\kappa^2 + 192\kappa)^{1/2}\}^{1/3} + 2}{8} \quad (16)$$

With a typical value of  $\kappa \sim 9$ , the predicted value of  $R_{asp,max}$  is about 7,<sup>8</sup> and the corresponding total growth time can be calculated as  $t_T \sim 550\text{s}$ . These values of  $R_{asp,max}$  and  $t_T$  are smaller than the experimental data 18 and 3600s, respectively, and the differences in the values of  $R_{asp,max}$  and  $t_T$  might result from the lower surface energy and higher work of adhesion of the nanorods growing in the gaseous phase and the existence



of an additional kinetic barrier for the elongated structures. Because there are unknown factors for the determining  $R_{asp,max}$ , further detailed investigation is needed. In the terminal stage of the growth, the nanorods of the aspect ratio that is larger than  $R_{asp,max}$  are depleted by the morphological transition from the rod-structures to a thin film accompanying decreasing total surface area.

### 3. Conclusions

We presented a theoretical model designed to explain the whole process of the noncatalytic growth of nanorods on a substrate. In the early stages of growth, the formation of the nuclei on the substrate is attributed to two mechanisms: cluster migration resulting from the surface diffusion of the adatoms and mass transport involving the coalescence and Ostwald ripening of the incident reaction precursors. In the 6-fold coordinated hexagonal lattice model of an array of the first settled adatoms, the most energetically favored cluster migration results in the 7-fold coalescence of the adatoms. After several growth steps (typically smaller than 6 steps), cluster migration ceases and this critical point is determined by the moment when the maximum translation time of the incident adatom (with the effective radius of  $R_1$ ) is larger than the mean free time of the adatom on the substrate. Once the growing nuclei on the substrate reach the thermodynamic size limit, a relatively slow reactant supply leads to 1D structure growth. This growth mechanism is mainly caused by the fact that a smaller reactant dose gives rise to a smaller interfacial energy in the anisotropic growth mechanism than in the isotropic growth mechanism. During the 1D growth of the nanorods, the growth rates of the radius and the height were calculated, and the height grows faster than the radius and, consequently, the aspect ratio of the nanorods also increases. In comparing it with the experimental results recently reported in the literature on ZnO nanorods, the proposed theoretical model was well matched with the experimental observations. We expect the presented work to help obtain a deeper insight into and the utilization of nanorods synthesized by vapor-phase transport reaction.

### References and Notes

- (1) Gudiksen, M. S.; Lieber, C. M. *J. Am. Chem. Soc.* **2000**, *122*, 8801.
- (2) Wu, Y.; Yang, P. *J. Am. Chem. Soc.* **2001**, *123*, 3165.
- (3) Huang, Y.; Duan, X.; Cui, Y.; Lauhon, L.; Kim, K.; Lieber, C. M. *Science* **2001**, *294*, 1313.
- (4) Park, W. I.; Yi, G. C.; Kim, M.; Pennycook, S. J. *Adv. Mater.* **2002**, *14*, 1841; Park, W. I.; Kim, D. H.; Sung, S. W.; Yi, G. C. *Appl. Phys. Lett.* **2002**, *80*, 4232.
- (5) Kwon, S. J.; Park, J. H.; Park, J. G. *Appl. Phys. Lett.* **2005**, *87*, 133112.
- (6) Tan, T. Y.; Li, N.; Gösele, U. *Appl. Phys. Lett.* **2003**, *83*, 1199.
- (7) Wang, C. X.; Wang, B.; Yang, Y. H.; Yang, G. W. *J. Phys. Chem. B* **2005**, *109*, 9966.
- (8) Kwon, S. J.; Park, J. G. *J. Chem. Phys.* **2005**, *122*, 214714.
- (9) Liu, Q. X.; Wang, C. X.; Yang, Y. H.; Yang, G. W. *Appl. Phys. Lett.* **2004**, *84*, 4568.
- (10) Liu, Q. X.; Wang, C. X.; Xu, N. S.; Yang, G. W. *Phys. Rev. B* **2005**, *72*, 085417.
- (11) Wagner, R. S.; Ellis, W. C. *Appl. Phys. Lett.* **1964**, *4*, 89.
- (12) Ohring, M. *Materials Science of Thin Films: Deposition and Structure*, 2nd ed.; Academic Press: San Diego, 2002.
- (13) Lifshitz, I. M.; Slyozov, V. V. *J. Phys. Chem. Solids* **1961**, *19*, 35.
- (14) Wagner, C. Z. *Elektrochem.* **1961**, *65*, 581.
- (15) Israelachvili, J. N. *Intermolecular and Surface Forces*, 2nd ed.; Academic Press: New York, 1992.
- (16) Kashchiev, D. *Surf. Sci.* **1979**, *86*, 14.
- (17) To calculate  $t_1$ , we used a typical deposition rate of semiconductor thin film by low-pressure MOCVD (LP-MOCVD) such that 280 Å/s at  $T = 1000\text{K}$ .<sup>10</sup> Using  $R_1 \sim 1.58 \times 10^{-10}\text{m}$  and  $d_1 \sim 3.55 \times 10^{-10}\text{m}$ , we could obtain the value of  $t_1$ ,  $t_1 = (300\pi \times 1.58^3)/(12\sqrt{3} \times 3.55^2 \times 280) \sim 5 \times 10^{-2}\text{s}$ .
- (18) Givargizov, E. I. *J. Cryst. Growth* **1975**, *31*, 20.
- (19) Wang, C. X.; Yang, Y. H.; Xu, N. S.; Yang, G. W. *J. Am. Chem. Soc.* **2004**, *126*, 11303; Wang, C. X.; Chen, J.; Yang, G. W.; Xu, N. S. *Angew. Chem., Int. Ed.* **2005**, *44*, 7414.
- (20) Witt, F.; Vook, R. W. *J. Appl. Phys.* **1968**, *39*, 2773.
- (21) Pelleg, J.; Zerlin, L. Z.; Lungu, S. *Thin Solid Films* **1991**, *117*, 197.
- (22) Oskam, G.; Nellore, A.; Penn, R. L.; Searson, P. C. *J. Phys. Chem. B* **2003**, *107*, 1734.
- (23) Oskam, G.; Hu, Z.; Penn, R. L.; Pesika, N.; Searson, P. C. *Phys. Rev. B* **2002**, *66*, 011403.
- (24) Ataev, B. M.; Lundin, W. V.; Mamedov, V. V.; Bagamadova, A. M.; Zavarin, E. E. *J. Phys.-Condens. Matter.* **2001**, *13*, L211.